Simulation of Argon Plasma Flows in Magnetoplasmadynamic Thrusters

IEPC-2007-281

Presented at the 30th International Electric Propulsion Conference, Florence, Italy
September 17-20, 2007

M.H. Moghimi* and M. Farshchi†
Aerospace Engineering Department, Sharif University of Technology, Tehran, Iran

Abstract: A two dimensional flow solver using the Roe averaging scheme to compute plasma flows for electromagnetic propulsion systems has been developed. The solver includes conservative equations of mass, momentum, energy and magnetic flux. Real equations of state, a multi-level ionization model, an anomalous transport model are implemented. These models are essential for a realistic simulation of MPD flow fields. The solver has been validated and the ability of this scheme to capture discontinuities has been demonstrated using standard test problems such as one dimensional Riemann problem. The solver is then used to simulate plasma flow in a real MPD thruster configuration. The ability of the code to model real geometry effects was confirmed by the excellent agreement between the predicted current contours around the anode lip with that measured experimentally.

Nomenclature

$\mathbf{B}$	=	magnetic induction
$\mathbf{E}$	=	electric field
$\bar{\bar{E}}_{res}$	=	resistivity tensor
ε	=	energy density
e	=	charge of electron
J	=	discharge current
$\mathbf{j}$	=	current density
k_{th}	=	coefficient thermal conduction
k_B	=	Boltzmann's constant
m	=	mass of a particle
n	=	number density of an species
p	=	pressure
$\mathbf{q}$	=	energy flux
T	=	temperature
$\mathbf{u}$	=	fluid velocity
η	=	resistivity
μ_0	=	permeability of free space
v	=	collision frequency
ρ	=	mass density

* Graduate Student, Aerospace Engineering Department, m_moghimi@ae.sharif.edu.
† Professor, Aerospace Engineering Department, farshchi@sharif.edu.

I. Introduction

The inability of chemical propulsion systems to achieve higher exhaust velocities is due to the limitation in the maximum tolerable temperature in the combustion chamber beyond which excessive heat transfer occurs to the chamber walls. There is also an intrinsic limitation on the maximum energy that is available from the chemical reactions. Both these limitations can be overcome by the use of electric propulsion. Two distinct means to harness electrical power to accelerate propellants can be identified: 1) Heating the propellant locally, such that average temperatures are higher than those that can be tolerated by the walls, 2) Acceleration of the propellant by the application of body forces. The first method can be explained by considering that the electrical power deposited per unit volume of the plasma is,

$$\mathbf{j}.\mathbf{E} = \left\{\eta j^2\right\} + \left\{(\mathbf{j}\times\mathbf{B}).\mathbf{u}\right\} \tag{1}$$

By maximizing the first term, the ohmic heating, the electrical power can be used to increase the enthalpy of the propellant in a localized fashion, thus avoiding excessive temperatures near the walls. This allows for the average chamber temperature to be higher than those attainable in chemical propulsion systems. The enthalpy can be recovered and converted into directed kinetic energy using a nozzle, as in a chemical rocket. This is the acceleration mechanism in electrothermal thrusters such as arcjets, resistojets and microwave-heated thrusters.

The second acceleration method relies on bypassing thermal expansion altogether, via application of direct body forces. This can be achieved by forces exerted by electrical and magnetic fields on an ionized gas:

$$\mathbf{f}_{ext} = \left\{\rho_e\mathbf{E}\right\} + \left\{\mathbf{j}\times\mathbf{B}\right\} \tag{2}$$

From Eq. (2) two distinct means of application of body forces can be identified. The first term is the body force due to an external electric field. This is the acceleration mechanism in electrostatic thrusters such as ion thrusters and field emission thrusters. For a highly conducting, quasi-neutral working fluid, the first term is small, compared to the second, the electromagnetic body force. This is the driving force in electromagnetic thrusters such as magnetoplasmadynamic thrusters, and pulsed plasma thrusters. The energy expended in this process is given by the second term in Eq. (1). It is important to note that, although the various means for using electrical power to accelerate gases has been explained in a conceptual fashion, the discovery of these methods was often empirical. For instance, magnetoplasmadynamic acceleration was discovered when an arcjet was operated under conditions of very low mass-flow rates and high currents, at which the second term of Eq. (1), dominated the first. Though the advantage of electric propulsion, the ability to provide higher exhaust velocities, is immediately noticeable, so are its two major limitations. First, in order to provide the required electrical power, an on board power supply has to be carried along. Therefore, the problem now becomes that of minimizing the combined mass of the power supply and the mass of the propellant, instead of merely the latter. The required propellant mass decreases with increasing exhaust velocity. However, for a system that provides a constant thrust, at a constant efficiency, the mass of the power supply increases with increasing exhaust velocity. Thus, the exhaust velocity should be at an optimum value that minimizes the combined mass of propellant and power supply. Second, all electric propulsion systems are intrinsically thrust limited because it is not practically feasible to supply electric power of the same order as that available from chemical/nuclear reactions. However, they are well-suited for missions where the instantaneous thrust requirements are small, but the total impulse requirement is large.

The MPD thruster has the unique capability, among all developed electric thrusters, of processing megawatt power levels in a simple, small and robust device. These features render it an attractive option for high energy deep space missions requiring higher thrust levels than other electric propulsion systems, such as piloted and cargo missions to Mars and other outer planets, as well as for near-term missions such as transfer from LEO to GEO.

The simple explanation for the acceleration mechanism described earlier oversimplifies the complexity that underlies the electromagnetic acceleration process, which embodies interlocking aspects of compressible gas dynamics, ionized gas physics, electromagnetic field theory, particle electrodynamics and plasma physics. To expand our understanding of the details of processes by which the electrical energy is partitioned among various energy sinks,

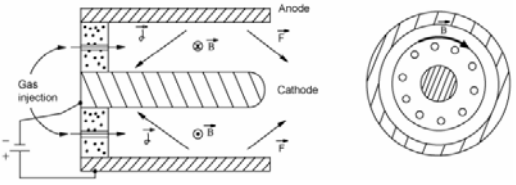

Figure 1. Schematic of a MPD thruster.

including acceleration, simple experimental models and corresponding numerical simulations and parametric studies are required. A simple laboratory model has been developed which would be used here as a model for our numerical studies.

In this model MPD thruster, a working fluid such as argon is heated by an electric discharge between two electrodes, as shown in Fig. 1. The total thrust of an MPD engine is composed of a magnetodynamic component, resulting from the interaction of the discharge current J and its self-field induced azimuthal magnetic induction field B_θ, and a thermodynamic component from the expansion of the ohmically heated propellant in the nozzle. In this work we assume that the thruster is axially symmetric, with no azimuthal current, resulting in a magnetic field with only an azimuthal component.

There have been several notable attempts to develop multi-dimensional models for MPD thruster flow fields. Some of them will be summarized below.

Caldo and Choueiri[1,2] carried out a two temperature model to study the effects of anomalous transport on MPD flows. The effort by Lapointe[3] was aimed at simulating plasma flows in existing thrusters, specifically Univ. Stuttgart's ZT-1 thruster and Princeton's Half-Scaled Flared Anode Thruster (HSFAT). An attempt to understand geometric scaling issues was also made in this work. Martinez-Sanchez[4,5] have developed two-temperature axisymmetric numerical models to study various aspects of the flow. Kubota and Okuno[6] use a Lax-Friedrich scheme, although a simplified model without viscosity and thermal conduction for simulating MPD flows. Sankaran and Choueiri[7] developed a high order accurate solver that captures MHD shocks monotonically and works reliably for strong magnetic fields. For this purpose they use a characteristics-based scheme for the MHD equations, with flux limiters to improve spatial accuracy. The present work aims to simulate MPD flows in a simple geometry,[1,7] without multistage schemes and flux limiters[6]. Our results are in general agreement with Sankaran's work. The maximum discharge current for which we could get a converged solution is 15kA.

II. Governing Equations

The computer program developed in this work presents a numerical scheme for resistive MHD equations, and assumes that the flow is fully ionized and the plasma is quasineutral. The full set of equations can be written as follows:

Mass conservation:

$$\frac{\partial \rho}{\partial t} + \nabla.(\rho \mathbf{u}) = 0 \tag{3}$$

Momentum conservation:

$$\frac{\partial \rho \mathbf{u}}{\partial t} + \nabla.\left(\rho \mathbf{u}\mathbf{u} + \bar{\bar{p}} - \bar{\bar{\beta}}_M \right) = \nabla.\bar{\bar{\tau}}_{vis} + \mathbf{B}(\nabla.\mathbf{B}) \tag{4}$$

Equation of magnetic flux:

$$\frac{\partial \mathbf{B}}{\partial t} + \nabla.(\mathbf{u}\mathbf{B} - \mathbf{B}\mathbf{u}) = \nabla.\bar{\bar{E}}_{res} + \mathbf{u}(\nabla.\mathbf{B}) \tag{5}$$

Energy conservation:

$$\frac{\partial \varepsilon}{\partial t} + \nabla.\left[(\varepsilon + p)\mathbf{u} - \bar{\bar{\beta}}_M .\mathbf{u} \right] = \nabla.\left[\frac{-\mathbf{E}' \times \mathbf{B}}{\mu_0} + \bar{\bar{k}}_{th} .\nabla T \right] + \left(\frac{\mathbf{B}}{\mu_0} .\mathbf{u} \right)(\nabla.\mathbf{B}) \tag{6}$$

Full set of equations can be shown as below:

$$\frac{\partial}{\partial t}\begin{bmatrix} \rho \\ \rho \mathbf{u} \\ \mathbf{B} \\ \varepsilon \end{bmatrix} + \nabla.\begin{bmatrix} \rho \mathbf{u} \\ \rho \mathbf{u}\mathbf{u} + \bar{\bar{p}} - \bar{\bar{\beta}}_M \\ \mathbf{u}\mathbf{B} - \mathbf{B}\mathbf{u} \\ (\varepsilon + p)\mathbf{u} - \bar{\bar{\beta}}_M .\mathbf{u} \end{bmatrix} = \nabla.\begin{bmatrix} 0 \\ 0 \\ \bar{\bar{E}}_{res} \\ \mathbf{q}_{diss} \end{bmatrix}. \tag{7}$$

The nature of the convective terms is hyperbolic and the nature of the dissipations terms is parabolic. For the case under consideration the relation for conservation of momentum of the plasma is analogous to the Navier-Stokes momentum equation, with external body force on the fluid. The energy density is the sum of internal, kinetic and magnetic field energies:

$$\varepsilon = \frac{p}{\gamma - 1} + \frac{1}{2}\rho \mathbf{u}.\mathbf{u} + \frac{B^2}{2\mu_0}. \tag{8}$$

For Faraday's law, the tensor $\bar{\bar{E}}_{res}$ satisfies the relation:

$$\nabla.\bar{\bar{E}}_{res} = -\nabla \times \left(\mathbf{E}^{'}\right), \tag{9}$$

where $\mathbf{E}^{'} = \eta \mathbf{j} + \left(\mathbf{j} \times \mathbf{B} - \nabla p_e\right)/ne$ is a relation for Ohm's law for the electric field in the plasma reference frame. This quantity also appears in the parabolic term of the energy equation, $\nabla.\mathbf{q}_{diss}$ along with thermal conduction:

$$\mathbf{q}_{diss} = \frac{\mathbf{B} \times \mathbf{E}^{'}}{\mu_0} + \bar{\bar{k}}_{th}.\nabla T. \tag{10}$$

In the momentum and energy equation $\bar{\bar{\beta}}_M = \left(1/\mu_0\right)\left[\mathbf{BB} - \left(B^2/2\right)\bar{\bar{I}}\right]$ is the Maxwell stress tensor. This tensor satisfies the relation,

$$\nabla.\bar{\bar{\beta}}_M = \mathbf{j} \times \mathbf{B}. \tag{11}$$

The external source in energy equation is clearly power per unit volume, $\dot{q} = \mathbf{j}.\mathbf{E}$, that can be show as below

$$\mathbf{j}.\mathbf{E} = -\left[\frac{\partial}{\partial t}\left(B^2/2\mu_0\right) + \nabla.\frac{(\mathbf{E} \times \mathbf{B})}{\mu_0}\right], \tag{12}$$

where the first term can be identified as the rate of change of energy density in the magnetic field, and the second term is the Poynting flux of electromagnetic energy.[8]

Because of the disparity between electron and ion temperatures we need to solve one of the species energy equations. These energy equations have the following form:[9]

$$\frac{\partial \varepsilon_e}{\partial t} + \nabla.\left[\varepsilon_e \mathbf{u}\right] + p_e \nabla.\mathbf{u} = \eta j^2 - \Delta \dot{\varepsilon} ie + \nabla.\left(\bar{\bar{k}} th,e .\nabla T_e\right) \tag{13}$$

$$\frac{\partial \varepsilon_i}{\partial t} + \nabla.\left[\varepsilon_i \mathbf{u}\right] + p_i \nabla.\mathbf{u} = \Delta \dot{\varepsilon} ie + \nabla.\left(\bar{\bar{k}} th,i .\nabla T_i\right). \tag{14}$$

In this work we solve electron energy equation Eq. (13), to compute electron temperature. It was also assumed that Ohmic heating, ηj^2, primarily affects the electrons. The rate of exchange of energy between the electrons and the ions, through collisions, can be estimated as,[7-9]

$$\Delta \dot{\varepsilon} ie = \frac{3\rho_e \nu_{ei}}{M_i} k_B \left(T_e - T_i\right). \tag{15}$$

So, the internal energy of ions can be calculated by subtracting the electron energy from the total energy of species. It is clear that at temperatures above 10^4 K, the deviations from the ideal gas model are significant.[6,10] This

relation for the equation of state will be used in the current model. As energy is deposited into the internal modes, the ratio of specific heats also changes. Further details can be found in appendix A.

It is imperative that, within the acceleration region, a significant fraction of the working fluid remains in a state of ionization, as the free charges are responsible for carrying current, and thereby establishing the electromagnetic fields required for acceleration. Irrespective of the manner in which the species are created, the densities of the electrons, n_e, ions, n_i, and the neutral, n_o, are related by the Saha equation,[11]

$$\frac{n_i n_e}{n_{i-1}} = \frac{2\left(2\pi m_e k_B T_e\right)^{3/2}}{h^3} \frac{\sum_l g_l^i e^{-\varepsilon_l^i / k_B T_e}}{\sum_l g_l^{i-1} e^{-\varepsilon_l^{i-1} / k_B T_e}} = K_i, \tag{16}$$

where h is Plank's constant, ε_l^i is the l^{th} energy level of the species of ionization level i, and g_l^i is the corresponding statistical weight. Even in the presence of thermal nonequilibrium between electrons and ions, a modified Saha equation can be applicable. For a model with N levels of ionization, the electron number density can be obtained by finding the single positive root of the polynomial,[11]

$$n_e^{N+1} + \sum_{l=1}^{N} \left[n_e^{N-1} \left(n_e - n_0 l \right) \prod_{m=1}^{l} K_m \right] = 0, \tag{17}$$

where equilibrium constant K_m is from Eq. (16).

The current can drive microinstabilities in the plasma thruster which may, through induced microturbulence, substantially increase dissipation and adversely impact the efficiency. Choueiri,[2,12] has developed a model to estimate the resulting anomalous transport and heating in terms of macroscopic parameters. Under this formulation, using the classical collision frequency of the particles, there exist additional momentum and energy transferring collisions between particles and waves. The resulting anomalous collision frequency is important whenever the ratio of electron drift velocity, u_{de}, to ion thermal velocity, v_{ti}, satisfies the following inequality:[13]

$$\frac{u_{de}}{v_{ti}} = \frac{j}{e n_e} \sqrt{\frac{M_i}{2 k_B T_i}} \geq 1.5. \tag{18}$$

The ratio of anomalous collision frequency, $\nu_{e,AN}$, to classical collision frequency, $\nu_{e,cl}$, was found to depend on the classical electron Hall parameter, Ω_e, and the ratio of ion to electron temperatures:

$$\frac{\nu_{e,AN}}{\nu_{e,cl}} = \left\{ 0.192 + 3.33\times10^{-2}\Omega_e + 0.212\Omega_e^2 - 8.27\times10^{-5}\Omega_e^3 \right\} + \frac{T_i}{T_e}\left\{ 1.23\times10^{-3} - 1.58\times10^{-2}\Omega_e - 7.89\times10^{-3}\Omega_e^3 \right\}. \tag{19}$$

The effective resistivity of the plasma can be expressed as:

$$\eta_{eff} = \frac{m_e\left(\nu_{e,cl} + \nu_{e,AN}\right)}{e^2 n_e}. \tag{20}$$

III. Axisymmetric Form of MHD Equations

In this section we proceed by writing the MHD system as a set of five scalar equations, and evaluating the divergence in cylindrical coordinates.

A. Scalar Variable Representation

The conservation form of the MHD equations, given in Eq. (7), describe the evolution of eight variables, namely the total density ρ, three components of momentum $(\rho u, \rho v, \rho w)$, three components of magnetic field (B_r, B_θ, B_z), and the total energy ε. However, in a self-field MPDT the magnetic field is purely azimuthal. Moreover, due to the

assumption of axisymmetry, azimuthal momentum can be neglected. These assumptions means that $B_r = B_z = 0$ and $\frac{\partial}{\partial \theta} = 0$. It is convenient to write the system of equations, Eq. (7), in a compact form

$$\frac{\partial \mathbf{U}}{\partial t} + \nabla . \bar{\bar{F}}_h = \nabla . \bar{\bar{F}}_p, \tag{21}$$

where $\mathbf{U}$ is the conserved variables vector of, $\bar{\bar{F}}_h$ is the tensor of hyperbolic convective fluxes, and $\bar{\bar{F}}_p$ is the tensor of parabolic dissipative fluxes.

Expanding the vector-tensor form of Eq. (7), in cylindrical coordinates along with the assumption stated above, the hyperbolic flux tensor is similarly expanded into 5 scalar equations:

$$\nabla . \bar{\bar{F}}_h = \frac{1}{r}\frac{\partial}{\partial r}\begin{bmatrix} r\rho u \\ r\left(\rho u^2 + p + \frac{B_\theta^2/2}{\mu_0}\right) \\ r(\rho w u) \\ r(u B_\theta) \\ r\left(\left(\varepsilon + p + \frac{B_\theta^2}{2\mu_0}\right)u\right) \end{bmatrix} + \frac{\partial}{\partial z}\begin{bmatrix} \rho w \\ \rho w u \\ \rho w^2 + p + \frac{B_\theta^2/2}{\mu_0} \\ w B_\theta \\ \left(\varepsilon + p + \frac{B_\theta^2}{2\mu_0}\right)w \end{bmatrix} + \frac{1}{r}\begin{bmatrix} 0 \\ -\left(p + \frac{B_\theta^2/2 - B_\theta^2}{\mu_0}\right) \\ 0 \\ -uB_\theta \\ 0 \end{bmatrix}. \tag{22}$$

The final derivative term, which arises from tacking the divergence of a tensor in cylindrical coordinates, is referred to as the geometric source term.

For the parabolic fluxes, we assume that $\mathbf{E}'$ may be calculated numerically. Eq. (9), is then written in terms of derivatives in cylindrical coordinates:

$$\nabla . \bar{\bar{E}}_{res} = -\nabla \times \mathbf{E}' = \begin{bmatrix} 0 \\ 0 \\ 0 \\ -\frac{\partial E_r'}{\partial z} + \frac{\partial E_z'}{\partial r} \\ \frac{1}{r}\frac{\partial (r q_r)}{\partial r} + \frac{\partial q_z}{\partial z} \end{bmatrix} = \begin{bmatrix} 0 \\ 0 \\ 0 \\ -\frac{\partial E_r'}{\partial z} \\ 0 \end{bmatrix} + \begin{bmatrix} 0 \\ 0 \\ 0 \\ \frac{\partial E_z'}{\partial r} \\ 0 \end{bmatrix} + \frac{1}{r}\begin{bmatrix} 0 \\ 0 \\ 0 \\ 0 \\ q_r \end{bmatrix} + \begin{bmatrix} 0 \\ 0 \\ 0 \\ 0 \\ \frac{\partial q_r}{\partial r} \end{bmatrix} + \begin{bmatrix} 0 \\ 0 \\ 0 \\ 0 \\ \frac{\partial q_z}{\partial z} \end{bmatrix}. \tag{23}$$

By using Eqs. (17), and (18), Eq. (7), would be expanded as below

$$\begin{aligned} &\frac{\partial}{\partial t}\begin{bmatrix} \rho \\ \rho u \\ \rho w \\ B_\theta \\ \varepsilon \end{bmatrix} + \frac{\partial}{\partial r}\begin{bmatrix} \rho u \\ \rho u^2 + p + \frac{B^2}{2\mu_0} \\ \rho u w \\ u B_\theta - E_z' \\ \left(\varepsilon + p + \frac{B^2}{2\mu_0}\right)u - q_r \end{bmatrix} + \frac{\partial}{\partial z}\begin{bmatrix} \rho w \\ \rho u w \\ \rho w^2 + p + \frac{B^2}{2\mu_0} \\ w B_\theta + E_r' \\ \left(\varepsilon + p + \frac{B^2}{2\mu_0}\right)w - q_z \end{bmatrix} = \begin{bmatrix} 0 \\ 0 \\ 0 \\ -\frac{\partial E_r'}{\partial z} + \frac{\partial E_z'}{\partial r} \\ \frac{1}{r}\frac{\partial (r q_r)}{\partial r} + \frac{\partial q_z}{\partial z} \end{bmatrix} = -\frac{1}{r}\begin{bmatrix} 0 \\ -\left(p + \frac{B^2/2 - B_\theta^2}{\mu_0}\right) \\ 0 \\ -uB_\theta \\ 0 \end{bmatrix} \\ &+\frac{1}{r}\begin{bmatrix} -(\rho u) \\ -\left(\rho u^2 + p + \frac{B^2}{2\mu_0}\right) \\ -(\rho u w) \\ -(u B_\theta) \\ -\left(\left(\varepsilon + p + \frac{B^2}{2\mu_0}\right)u\right) \end{bmatrix} + \frac{1}{r}\begin{bmatrix} 0 \\ 0 \\ 0 \\ 0 \\ q_r \end{bmatrix} = \frac{1}{r}\begin{bmatrix} -(\rho u) \\ -\left(\rho u^2 + \frac{B_\theta^2}{\mu_0}\right) \\ -(\rho u w) \\ 0 \\ q_r - \left(\left(\varepsilon + p + \frac{B^2}{2\mu_0}\right)u\right) \end{bmatrix}. \end{aligned} \tag{24}$$

By some algebraic operations we could show the full set of equations as below:

$$\frac{\partial}{\partial t}\begin{bmatrix}\rho\\ \rho u\\ \rho w\\ B_\theta\\ \varepsilon\end{bmatrix}+\frac{\partial}{\partial r}\begin{bmatrix}\rho u\\ \rho u^2+p+\dfrac{B^2}{2\mu_0}\\ \rho uw\\ uB_\theta-E_z^{'}\\ \left(\varepsilon+p+\dfrac{B^2}{2\mu_0}\right)u-q_r\end{bmatrix}+\frac{\partial}{\partial z}\begin{bmatrix}\rho w\\ \rho uw\\ \rho w^2+p+\dfrac{B^2}{2\mu_0}\\ wB_\theta+E_r^{'}\\ \left(\varepsilon+p+\dfrac{B^2}{2\mu_0}\right)w-q_z\end{bmatrix}=\frac{1}{r}\begin{bmatrix}-(\rho u)\\ -\left(\rho u^2+\dfrac{B_\theta^2}{\mu_0}\right)\\ -(\rho uw)\\ 0\\ q_r-\left(\left(\varepsilon+p+\dfrac{B^2}{2\mu_0}\right)u\right)\end{bmatrix}. \tag{25}$$

The parabolic component of the energy equation can also be expressed in this form,

$$\nabla.\mathbf{q}=\frac{1}{r}\frac{\partial(rq_r)}{\partial r}+\frac{1}{r}\frac{\partial(q_\theta)}{\partial\theta}+\frac{\partial q_z}{\partial z}, \tag{26}$$

where the component of $\mathbf{q}$, as defined in Eq. (10), can be written:

$$q_r=-\frac{E_\theta^{'}B_z-E_z^{'}B_\theta}{\mu_0}+k\frac{\partial T}{\partial r} \tag{27}$$

$$q_\theta=-\frac{E_z^{'}B_r-E_r^{'}B_z}{\mu_0}+k\frac{1}{r}\frac{\partial T}{\partial\theta} \tag{28}$$

$$q_z=-\frac{E_r^{'}B_\theta-E_\theta^{'}B_r}{\mu_0}+k\frac{\partial T}{\partial z}. \tag{29}$$

With the assumptions used in this work it is clear that $q_\theta=0$. Also the other components could be written:

$$q_r=\frac{E_z^{'}B_\theta}{\mu_0}+k\frac{\partial T}{\partial r}=\frac{E_z^{'}B_\theta}{\mu_0}+k_{th,e}\frac{\partial T_e}{\partial r}+k_{th,h}\frac{\partial T_i}{\partial r} \tag{30}$$

$$q_z=-\frac{E_r^{'}B_\theta}{\mu_0}+k\frac{\partial T}{\partial z}=-\frac{E_r^{'}B_\theta}{\mu_0}+k_{th,e}\frac{\partial T_e}{\partial z}+k_{th,h}\frac{\partial T_i}{\partial z}. \tag{31}$$

Eqs. (25), (30), and (31), are solved in combination with electron energy equations at every time level, for a given set of initial and boundary conditions.[14-18]

IV. Numerical Simulation

Despite several earlier efforts in the front of MPDT flow simulation, there remains a need for an accurate and robust numerical scheme. First, some fundamental concepts pertaining to the guiding principles to be used in this thesis will be reviewed. Then, the characteristics-splitting technique for the solution of convection equations will be developed and validated. That will be followed by a brief discussion of the well known techniques for the solution of the diffusion equations.

A. Hyperbolic Equations

1. Spatial Discretization

The numerical solution to the set of hyperbolic equations without the diffusion terms is based on techniques that are used in computational fluid dynamics. The method can be explained using Eq. (7), in one dimension,

$$\frac{d\mathbf{U}_j}{dt}+\frac{\mathbf{Hz}_{j+1/2}-\mathbf{Hz}_{j-1/2}}{\Delta z}=0, \tag{32}$$

where, **U** is the vector of conserved variables, and Hz is the approximation of flux in the z direction.
The true flux, obtained from Eq. (7), in the z direction can be split as,

$$\mathbf{Fz}(\mathbf{U})=\mathbf{Fz}(\mathbf{U})^{+}+\mathbf{Fz}(\mathbf{U})^{-}, \tag{33}$$

where the eigenvalues of $d\mathbf{Fz}^{+}/d\mathbf{U}$ are all non-negative, and the eigenvalues of $d\mathbf{Fz}^{-}/d\mathbf{U}$ are all non-positive. Then, the approximation of flux is estimated as,

$$\mathbf{Hz}_{j+\frac{1}{2}} = \mathbf{Fz}_{j}^{+} + \mathbf{Fz}_{j+1}^{-}. \tag{34}$$

Using Eq. (33), this can be rewritten as,

$$\mathbf{Hz}_{j+\frac{1}{2}} = \frac{1}{2}\left(\mathbf{Fz}_{j} + \mathbf{Fz}_{j+1}\right) - \mathbf{Dz}_{j+\frac{1}{2}}, \tag{35}$$

where

$$\mathbf{Dz}_{j+\frac{1}{2}} = \frac{1}{2}|\mathbf{A}|\Delta\mathbf{U}_{j+1/2}. \tag{36}$$

In Eq. (36), $\Delta\mathbf{U}_{j+1/2} = \mathbf{U}_{j+1} - \mathbf{U}_{j}$ and $\mathbf{A} \equiv \mathbf{R}\boldsymbol{\Lambda}\ \mathbf{R}^{-1}$, also $\mathbf{R}$ contains the right eigenvectors of $\mathbf{A}$ as its columns, and $\mathbf{R}^{-1}$ contains the left eigenvectors of $\mathbf{A}$ as its rows. $\boldsymbol{\Lambda}$ is the diagonal matrix of eigenvalues of $\mathbf{A}$. Since $\boldsymbol{\Lambda}$ can be easily split into,[19-21]

$$\boldsymbol{\Lambda} = \boldsymbol{\Lambda}^{+} + \boldsymbol{\Lambda}^{-}. \tag{37}$$

By using Eq. (37), $\mathbf{A}$ can be show as $\mathbf{A}^{\pm} \equiv \mathbf{R}\boldsymbol{\Lambda}^{\pm}\mathbf{R}^{-1}$. Then $|\mathbf{A}|$ defines as $|\mathbf{A}| = \mathbf{A}^{+} - \mathbf{A}^{-}$.
Similar equations can be written for the corresponding terms in the r direction.

B. Verification

The test problem chosen to validate this scheme consists of testing the Brio-Wu MHD shock tube problem. Two stationary plasma are separated by a membrane which is removed at t=0, allowing the plasma to interact. The boundary conditions for the problem are outflow boundary condition with the initial data given by,

$$\begin{aligned} Left &\left[\rho=1.0, V_x=0.0, V_y=0.0, V_z=0.0, B_x=\frac{3}{4}, B_y=1.0, B_z=0.0, p=1.0\right]^{T} \\ Right &\left[\rho=\frac{1}{8}, V_x=0.0, V_y=0.0, V_z=0.0, B_x=\frac{3}{4}, B_y=-1.0, B_z=0.0, p=\frac{1}{10}\right]^{T}. \end{aligned} \tag{38}$$

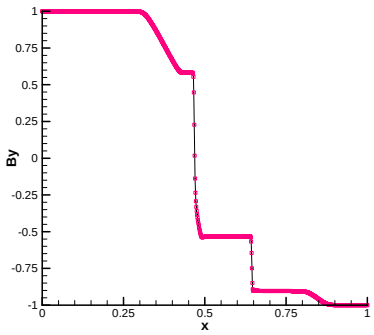

Figure 2. Comparison of calculated profiles of magnetic field with exact solution.

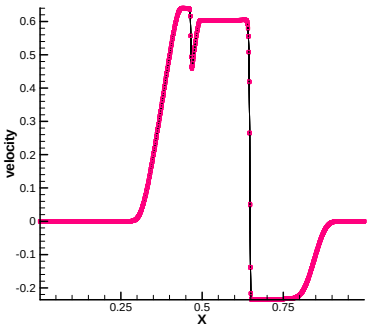

Figure 3. Comparison of calculated profiles of velocity with exact solution.

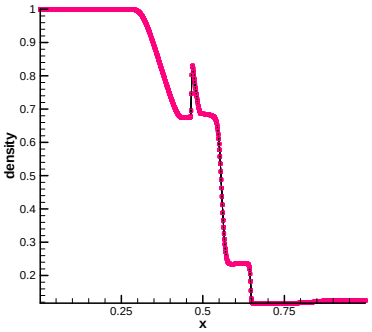

Figure 4. Comparison of calculated profiles of density with exact solution.

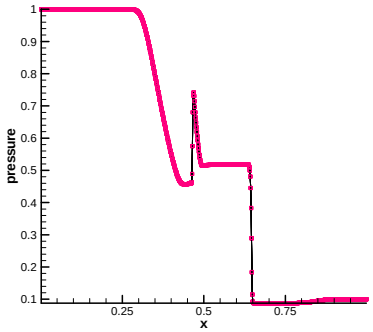

Figure 5. Comparison of calculated profiles of pressure with exact solution.

The number of points in the domain, and the time were chosen to allow comparisons to other works.[22] As seen in these figures, the scheme successfully captures the time-dependent discontinuities. In the above figures the solid line represents the exact solution and the red dots represent the numerical results, respectively.

C. Parabolic Equations

1. Spatial Discretization

Numerical methods for parabolic equations are relatively commonplace. Parabolic terms can be written as,

$$\mathbf{S}_{dis} = \nabla.\begin{bmatrix} 0 \\ \bar{\bar{\tau}}_{vis} \\ \bar{\bar{E}}_{res} \\ \mathbf{q} \end{bmatrix}, \tag{39}$$

where

$$\nabla.\bar{\bar{\tau}}_{vis} = \nabla.\left[\mu_{vis}\nabla\mathbf{u}\right], \tag{40}$$

represents the loss of momentum due to viscous forces,

$$\nabla.\bar{\bar{E}}_{res} = -\nabla\times\left[\frac{\bar{\bar{\eta}}.(\nabla\times\mathbf{B})}{\mu_0}\right], \tag{41}$$

represents the resistive diffusion of the magnetic flux, including the Hall effect, and,

$$\nabla.\mathbf{q}_{diss} = \nabla.\left[\bar{\bar{\tau}}.u - \frac{\mathbf{B}\times\mathbf{E}'}{\mu_0} + \bar{\bar{k}}_{th}.\nabla T\right]. \tag{42}$$

represents the energy source/sinks due to viscous heating, Ohmic heating, and thermal conduction respectively. These equations require second-order accurate in space. Therefore, a simple central-differencing scheme will be sufficient for this problem.

2. Temporal Discretization

Physical dissipation brings in different characteristic time scales into the problem. They are:

Viscous diffusion $= \rho\Delta r^2/\mu_{visc}$ $\sim 10^{-9}s$

Magnetic diffusion $= \mu_0\Delta r^2/\eta$ $\sim 10^{-10}s$

Heat conduction $= n_e k_B \Delta r^2/k_{th}$ $\sim 10^{-9}s.$

D. Starting Values and Boundary Conditions

Code input consists of the thruster discharge current, propellant mass flow rate, geometric boundary conditions, background gas pressure, and initial estimates for the plasma transport coefficients. Ion and electron temperatures are typically set to 3000K at electrode surfaces. Vacuum tank pressures are set $_{10^{-4}}$ torr. The inlet velocity is assumed to be sonic and uniform at the backplate. The inlet density is assumed to be uniform and is calculated from the continuity equation. Radial velocities are initially set to zero, and are defined by symmetry to remain zero along the centerline. Initial temperatures throughout the calculation region are set to their values at the backplate. A no-slip boundary condition on velocity is employed at all insulator and electrode surfaces. The electrodes are modeled as equipotential surfaces. Electric fields which enter perpendicular to electrode surfaces satisfy the condition $\partial \mathbf{E} / \partial \mathbf{n} = 0$, where $\mathbf{n}$ denotes a unit vector normal to the surface. Electric fields lying along electrode surfaces are set to zero, consistent with equipotential surface boundary conditions. The magnetic stream line $\psi = rB_\theta$ is set equal to $-\mu_0 J / 2\pi$ along the backplate, zero along the centerline, and is assumed to be continuous at both the outer radial grid boundary and downstream axial grid boundary. Setting magnetic stream line equal to zero at the thruster exit plane would prevent the current from blowing out of the thruster, while setting magnetic stream line equal to zero at the downstream grid boundary might artificially compress the current blown downstream.

V. Results

The results shown in this section are for argon flowing at 6g/s and a discharge current of 15 kA. It is important to note that divergence always occurred through strong oscillations of the electron energy density in the time-stepping with the electron temperature going negative or increasing exponentially. The strongest term in the energy equation of electron is ηj^2, that grows as the square of the total current. The fact that the cause of the divergence always lies in the electron energy equation and the fact that the electron temperature increases asymptotically to unrealistic levels when divergence occurs are also indicative of the lack of proper representation of energy sinks in the electron energy. It is important to state that the inclusion of finite equilibrium rates in many processes and the inclusion of microturbulent effects on ionization[13] should render the electron energy equation more realistic and thus better behaved.

A. Density

The electron number densities within the chambers increases near the lower wall of the chamber that this increase may be related to the radial pumping force, $j_z B_\theta$, which pushes the plasma away from the anode, toward the cathode. This trend has been observed in experiments and in previous simulations .[1,7]

B. Ion Temperatures

The distribution of ion temperatures is shown in Fig. 7. Within the thrust chamber, temperature varies from about 0.6 to 2.5eV. The hottest region of the ion temperatures occurs at the centerline. The cathode tip is the other region that has this rang of the temperature. It could be related to stagnation. Another possible explanation could be that the axisymmetric assumption causes thermal conduction at the centerline to go to zero. If there are symmetry breaking oscillations in reality, then there would be thermal conduction that would reduce the temperature in that region.[1,7,23] Nevertheless, these numbers are in general agreement with measurements[7] at these operating conditions.

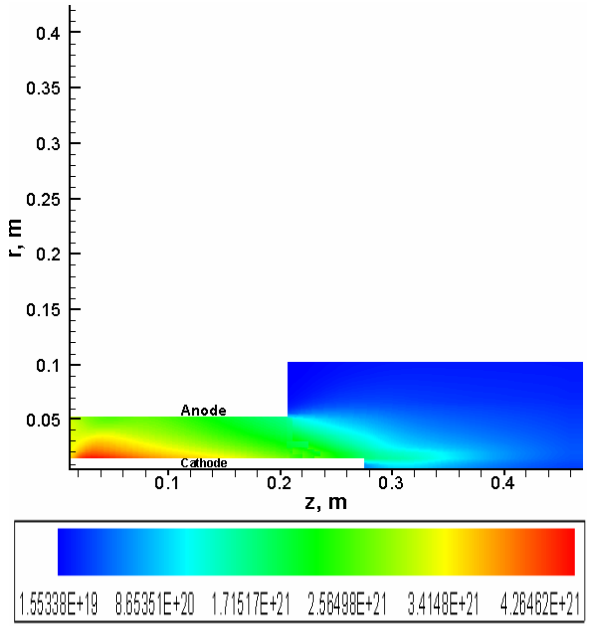

Figure 6. Distribution of electron number densities (particle/m^3).

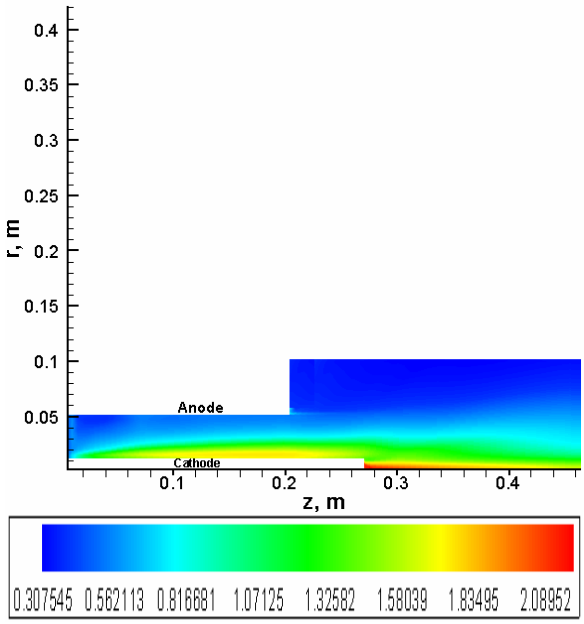

Figure 7. Distribution of ion temperatures (eV).

C. Magnetic Field & Enclosed Current

The spatial distribution of magnetic field strength in the domain is shown in Fig. 8. Magnetic field varies as inverse of the radius and decreases linearly with axial distance that shows clearly in Fig. 8. This is strictly true for a uniform current distribution in the channel. However, the current and magnetic field propagate downstream via convection and diffusion, and their distributions are no longer uniform. The contours of enclosed current are shown in Fig. 9. The current attachment is strongest near the backplate, and at the exit. This pattern is generally observed in many MPDT.[7,23]

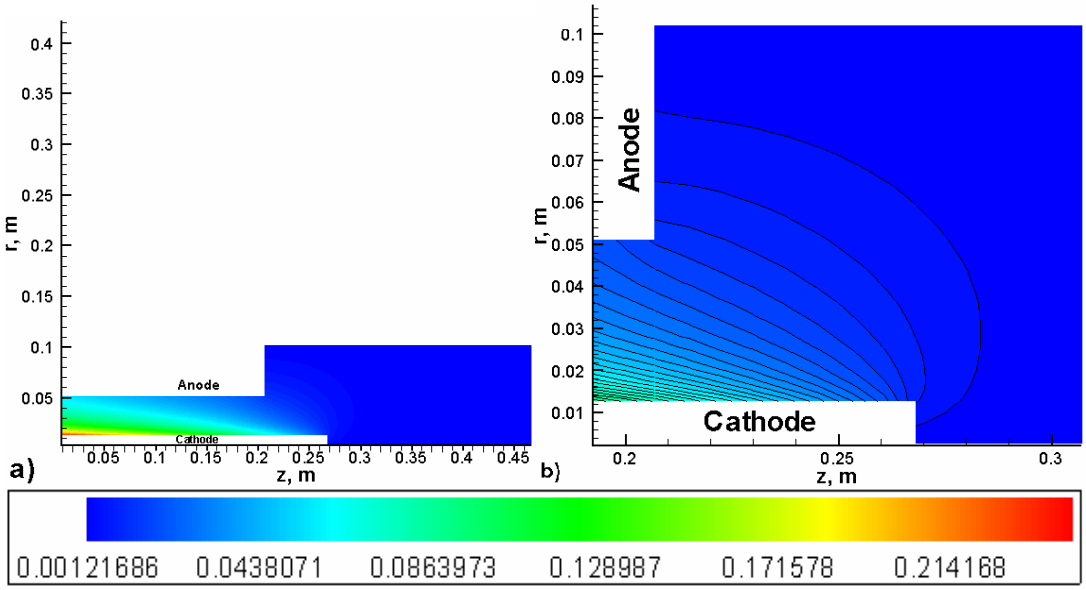

Figure 8. Distribution of magnetic field (T).

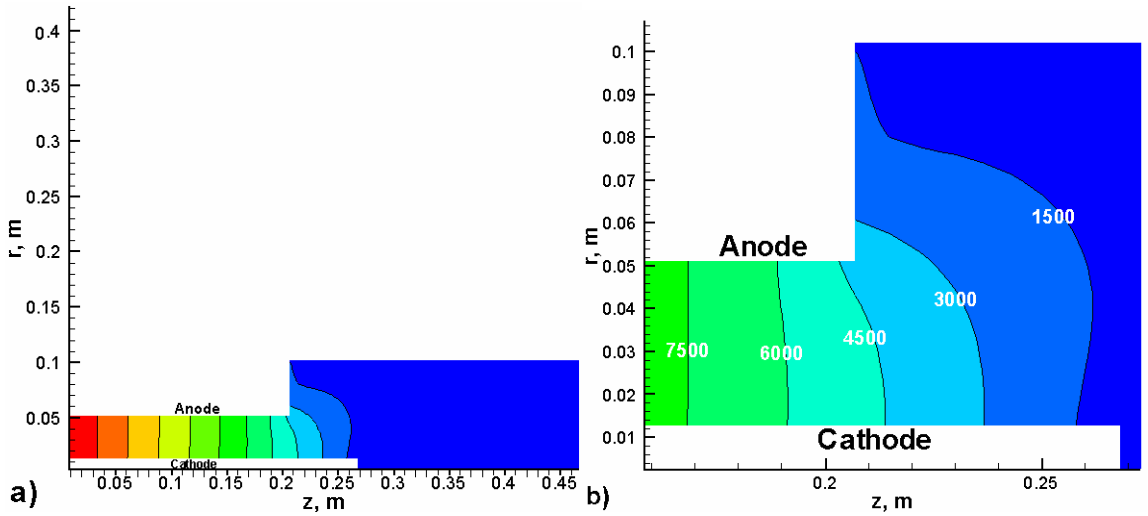

Figure 9. Distribution of enclosed current (A).

D. Hall Parameter & Anomalous Transport

The distribution of the electron Hall parameter in the domain is shown in Fig. 10. It varies from 0.3 to 1.2 in the thrust chamber. Since the magnetic field and species temperatures increase with decreasing radius, so does the Hall

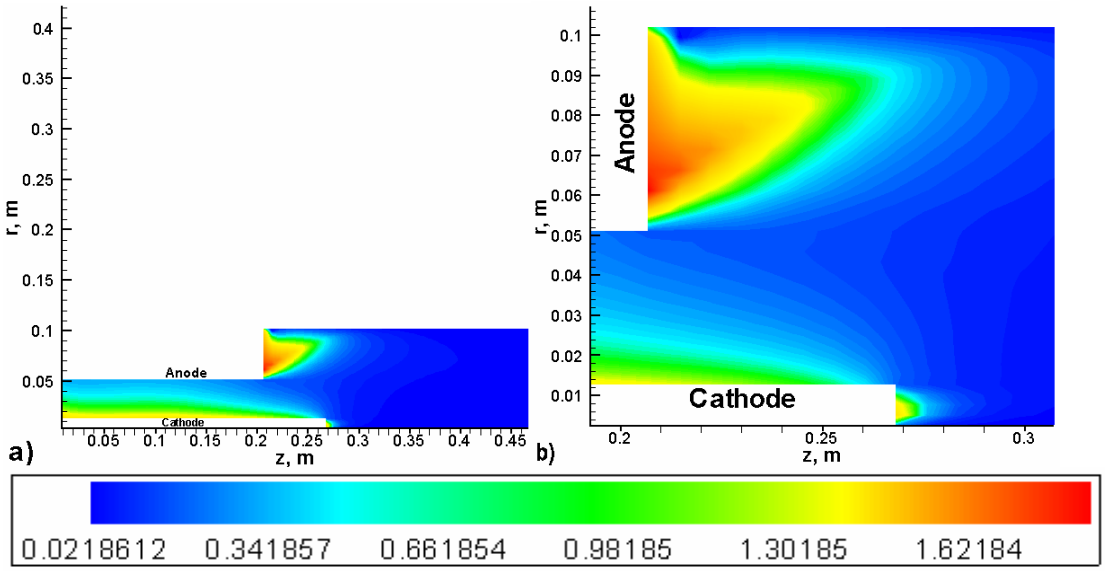

Figure 10. Distribution of Hall parameter.

parameter. The Hall parameter is higher at the electrode tips than in any other region. Once again, referring to Figs. 8, and 7, the magnetic field is higher (cyclotron frequency is higher) and temperatures are higher (collision frequency are lower) in those regions. These values of electron Hall parameters are substantially lower than values observed in other MPD thruster configurations. Unlike many MPD thruster configuration[6,7] in which the anode has a relatively small size at the exit of the thruster, here anode is along the thrust chamber, leading to a more diffusive current attachment pattern. The ratio of anomalous to classical resistivity is a strong function of the electron Hall parameter, beyond a cutoff, $\frac{u_{de}}{v_{ti}} \geq 1.5$.[11] Ratio of anomalous to classical resistivity is shown in Fig. 11. Due to low value of Hall parameter the overall effect of anomalous transport is limited. As shown in Fig. 11, due to high Hall

parameter at the tips of the electrodes and high ion temperatures in these regions the ratio of anomalous to classical resistivity is higher than other regions. As shown in Fig. 9, the pattern of the enclosed current is similar to a straight line within the channel. This is probably due to the larger average value of Hall parameter in the thrust chamber. Also this phenomenon could cause the rarefying of the pumping force. Then most of the $\mathbf{j}\times\mathbf{B}$ term is used as blowing force.

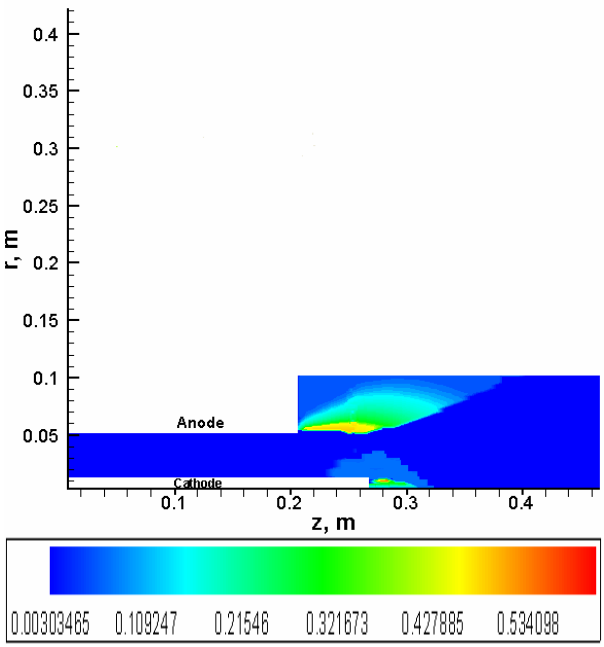

Figure 11. Ratio of anomalous to classical resistivity.

VI. Conclusion

The ability of the new code to model real geometry effects was confirmed by the excellent agreement of the predicted current contours around the anode lip with that measured experimentally. Also, the calculated contours of ion temperatures, density of electron particles, Hall effect and anomalous transport are in general agreement with previous work in this field of research. However the lack of proper convergence at large discharge current may be related to the ohmic term in the electron energy equation and the use of real equations of sate that causes the solution to be unrealistic and unstable.

Appendix A: Physical Models

Calculation of gama for real equation of state.

$$\gamma(T) = A + Be^{-((T-C)/D)^2}, \tag{A1}$$

Where for the temperature range of 800< T < 10000 we have A = 1.112166458, B = 0.5299556066, C = 8050606514, D = 1318851134, and for 10000< T < 40000 we have A = 1.105400732, B = 0.0252665935, C = 1514282094, and D = 2394061632.

References

[1]Caldo, G., Choueiri, E. Y., Kelly, A. J., and Jahn, R. G., "Numerical Fluid Simulation of an MPD Thruster with Real Geometry," Proceeding of the 23rd International Electric Propulsion Conference, Seattle, WA, 1993, pp. 93-072.

[2]Choueiri, E. Y., "Anomalous resistivity and Heating in Current-Driven Plasma Thrusters," Journal Physics of Plasmas, Vol. 6, No. 5, 1999, pp. 2290.

[3]LaPointe, M., "Numerical Simulation of Geometric Scale Effects in Cylindrical Self-Field MPD Thruster," NASA-CR-189224, 1992.

[4]Chanty, J. M. G., and Martinez-Sanchez M., "Two Dimensional Numerical Simulations of MPD Flows," AIAA-87-1090, 1987.

[5]Niewood, E. H., "An Explantion for Anode Voltage Drops in an MPD," PhD. thesis, MIT, 1993.

[6]Kubota, K., Funaki, I., Okuno, Y., "Numerical Simulation of a Self-Field MPD Thruster using Lax-Friedrich Scheme," Proceeding of ISSS-7, 26-31 March, 2005.

[7]Sankaran, K., Martinelli, L., Jardin, S. C., Choueiri, E. Y., "A Flux-Limited Numerical Method for Solving the MHD Equations to Simulate Propulsive Plasma Flows," International Journal for Numerical Methods in Engineering, Vol. 53, 2002, pp. 1415-1432.

[8]Sankaran, K., Choueiri, E. Y., Jardin, S. C., "Application of a New Numerical Solver to the simulation of MPD Flows," AIAA Paper 2000-3537,2000.

[9]Sankaran, K., Jardin, S. C., Choueiri, E. Y., "Parallelization and Validation of an MHD Code for the Simulation of Self-Field MPDT Flows," Proceeding of the 27th International Electric Propulsion Conference, 2001, pp. 01-127.

[10]Sparks, W. M., Fischel, D., "Partition Functions and Equations of State in Plasms," NASA SP-3066, 1971.

[11]Heiermann, J., Auweter-Kurtz, M., and Sleziona, P. C., "Adaptive Computation of the Current-Carrying Plasma in an MPD Rocket Thruster," Time-Dependent Magnetohydrodynamics: Analytical, Numerical, and Application Aspects, 1998.

[12]Choueiri, E. Y., "Instability of a Current-Carrying Finite-Beta Collisional Plasma," Physical Review E, Vol. 64, No. 6, 2001.

[13]Jahn, R. G., Physics of Electric Propulsion, McGraw-Hill, New York, 1968, Chap. 8., pp. 240-246.

[14]LaPointe, M. R., and Mikellides, P. G., "High Power MPD Thruster Development at the NASA Glenn Research Center," AIAA Paper 01-3499, 2001.

[15]Powell, K., "An approximation Riemann Solver for Magnetohydrodynamics (That works in more than one dimension)," Tech. Rep. ICASE Report 94-24, 1994.

[16]Powell, K., Roe, P., Linde, T., Gombosi, T., and Zeeuw, D. D., "A Solution-Adaptive Upwind Scheme for Ideal Magnetohydrodynamics," Journal of Computational Physics, Vol. 154, 1999, pp. 284-309.

[17]LeVeque, R., Finite Volume Method for Hyperbolic Problems, Cambridge University Press, 2002.

[18]Brackbill, J., and Branes, D., "The effect of nonzero $\nabla \cdot \mathbf{B}$ on the numerical solution of the magnetohydrodynmaic equations," Journal of Computational Physics, Vol. 35, 1980, pp. 426.

[19]Godunov, S. K., "Symmetric Form of the Equations of Magnetohydrodynamics," In Numerical Methods for Mechanics of Continuum Medium, Report of the Computer Center of the Siberian Branch of the USSR Academy of Science, 1972.

[20]Evans, E. and Haley, J., "Simulation of magnetohydrodynamic flows: A constrained transport method," The Astrophysical Journal , Vol. 332, 1988, pp. 659.

[21]Jones, O., Shumlak, U., and Eberhardt, S., "An Implicit Scheme For Non-Ideal Magnetohydrodynamics," Journal of Computational Physics, Vol. 130, 1997, pp. 231-242.

[22]Sod, G. A., "A Survey of Finite-Difference Method For Systems of Nonlinear Conservation Laws," Journal of Computational Physics, Vol. 27, No. 1, 1978.

[23]Villani, D. D., "Energy Loss Mechanism in a Magnetoplasmadynamic Arcjet," PhD. Thesis, Princeton University, 1987.